

Coupling between ferroelectric distortions and excitonic properties in PbTiO₃

Pietro Pacchioni,^{1,2} Lorenzo Varrassi,^{1,3} and Cesare Franchini^{4,1}

¹⁾*Dipartimento di Fisica e Astronomia, Università di Bologna, 40127 Bologna, Italy*

²⁾*Institute of Physics, École Polytechnique Fédérale de Lausanne (EPFL), 1015 Lausanne, Switzerland*

³⁾*CINECA National Supercomputing Center, Casalecchio di Reno, I-40033 Bologna, Italy*

⁴⁾*University of Vienna, Faculty of Physics, Center for Computational Materials Science, Vienna, Austria*

(Dated: December 3, 2025)

PbTiO₃ is a ferroelectric perovskite semiconductor with favourable electronic and optical properties, making it suitable for a wide range of applications, including photo-catalysis and (opto)electronic devices. Despite its relevance, an accurate *ab-initio* description of the optical absorption spectrum and of the impact of ferroelectric distortion on the excitonic properties is still lacking. We combine G_0W_0 and Bethe–Salpeter Equation calculations to investigate the electronic and optical properties of PbTiO₃, tracking the evolution of its excitonic spectrum along the transition from the cubic paraelectric to the tetragonal ferroelectric phase. As the polar distortion increases, the first absorption peak of the cubic phase splits into two distinct features due to symmetry breaking, which partially lifts the degeneracy of the underlying excitonic state. Crucially, the distortion further introduces an in-plane/out-of-plane anisotropy in the spectra and controls the energy separation between the resulting excitonic branches. These findings highlight the potential for tuning the optical absorption properties of PbTiO₃ via the application of an external electric field.

I. INTRODUCTION

Transition-metal-oxide (TMO) perovskites present a rich interplay of charge, spin, orbital and lattice degrees of freedom underpinning phenomena ranging from colossal magneto-resistance^{1,2} to multiferroicity³ and superconductivity^{4,5}, which have led to their employment in a variety of applications.

Among ferroelectric TMOs, PbTiO₃ (PTO) stands out thanks to its large spontaneous polarization^{6,7}, sizeable piezo-^{8,9} and electro-optic coefficients^{10,11} and the possibility of switching its tetragonal distortion with modest electric fields^{12,13}. These attributes make PTO a prototype platform for tunable opto-electronic devices, non-linear optical systems¹⁴ and solar cells applications¹⁵.

Despite growing interest, first-principles descriptions of the optical spectra of PbTiO₃ remain limited. Only a few studies report its absorption spectrum^{16–18}, with most relying on the independent-particle approximation or semi-empirical Hubbard corrections. These approaches neglect electron–hole interactions, which are known to be crucial for accurately reproducing experimental spectra^{19–21}. Moreover, only a limited number of studies incorporate a quasiparticle GW framework^{18,22}, despite its status as the state-of-the-art approach for modeling (ferroelectric) perovskites^{23–25}.

Furthermore, the cubic and tetragonal phases have traditionally been studied as distinct, isolated structures, leaving open the question of how the electronic, optical, and excitonic properties evolve continuously with the gradual onset of ferroelectric distortion. Such intermediate polar states are experimentally accessible through the application of an electric field^{26,27}, and may enable electric-field control of the light absorption spectrum.

An accurate description of the electronic and optical proper-

ties of materials requires both quasiparticle (QP) corrections beyond density functional theory (DFT) and a proper treatment of excitonic effects. Single-shot G_0W_0 calculations have proven predictive for perovskites^{20,24,25,28–30}, while solving the Bethe–Salpeter equation (BSE) enables the inclusion of electron–hole interactions, which are essential for accurately computing exciton binding energies and oscillator strengths^{31,32}. However, a fully self-consistent GW+BSE workflow on the dense k -point meshes required for convergence of excitonic energies remains computationally prohibitive³¹. A practical alternative is the model-BSE (mBSE) approach, where the screened Coulomb interaction is replaced by a physically motivated analytical model^{33–35}. Benchmark studies have demonstrated that mBSE can satisfactorily reproduce full GW+BSE spectra for TMOs while reducing the computational cost by orders of magnitude^{28,36}.

In this work, we address the aforementioned gaps by performing a systematic G_0W_0 + mBSE investigation of PbTiO₃ along a continuous ferroelectric distortion pathway, connecting the paraelectric cubic structure to the fully relaxed tetragonal phase. For seven intermediate configurations, we obtain orbital-projected band structures with converged G_0W_0 parameters, solve the mBSE on dense k -point grids to extract the optical absorption spectra, and trace the evolution of the fundamental, direct, and optical gaps, as well as the first bright and dark excitons. Our results reveal how the breaking of cubic symmetry lifts the triple degeneracy of the lowest exciton, leading to a polarization-dependent splitting of the first absorption peak.

This splitting of the first cubic absorption peak into two distinct features is correlated with the emergence of anisotropic exciton wavefunctions: one localized along the Γ –Z direction in k -space, and the other pinned at Γ . This behaviour provides a microscopic mechanism for tailoring optical selection rules through controlled ferroelectric displacements.

II. METHODS

All calculations were performed using the Vienna ab initio Simulation Package (VASP)^{37,38} with the projector-augmented wave method (PAW)³⁹. The GW versions of the potentials were used. Norm conserving (NC) potentials including the semicore states were used for the titanium atom to ensure accurate QP energies^{23,25,30}.

Ionic relaxation was performed for both the cubic and tetragonal structures of PTO at the DFT level, in the generalized gradient approximation (GGA) with Perdew, Burke and Ernzerhof (PBE) functionals⁴⁰. PBE is known to overestimate the tetragonal distortion of TMO perovskites^{29,41}, so the structural parameters were interpolated between the relaxed cubic and tetragonal structures, producing seven intermediate structures. A ferroelectric structure closely matching experiment (see Table I) was selected as representative of this phase of PTO in the absence of electric field. Details about the structures with higher tetragonal distortions are discussed in the Supplementary Materials (SM).

	a [Å]	c/a	Ω [Å ³]	Δ_{Ti}
Interpolated	3.926	1.069	64.66	0.034
Experiment	3.880 – 3.904	1.064 – 1.071	62.56 – 63.31	0.038

Table I: Lattice constant a , tetragonal distortion c/a , cell volume Ω and titanium ion displacement Δ_{Ti} for the selected interpolated tetragonal structure (Interpolated) compared to experiment. Experimental ranges from refs.^{42–45}

For all structures, the absorption spectra were determined following a procedure similar to that outlined in refs.^{25,28}:

1. An initial self-consistent DFT step is performed;
2. A single shot G_0W_0 calculation is performed by constructing the one particle Green's function from the single electron energies and orbitals determined in the previous step, while the screened Coulomb interaction is computed using the Random Phase Approximation (RPA)^{46,47}. The convergence procedure for the QP energies described in²⁵ was employed, leading to a requirement of 3200 virtual bands and a plane-wave energy cut-off of 900 eV for convergence to about 0.01 eV. The screened Coulomb interaction and the self-energy were represented with 100 frequency points.
3. The optical absorption spectra are calculated by solving the BSE using the mBSE approach in the Tamm-Damcoff approximation, starting from the G_0W_0 data.

Convergence of the k -grid is critical when solving the BSE^{48–50}. To ensure accurate results, multiple calculations of the absorption spectra of the cubic and tetragonal structures were performed with increasingly dense k -grids. No new peaks were verified to appear under 5 eV when employing a uniform, Γ -centred $16 \times 16 \times 16$ grid. Convergence was also verified with respect to the number of occupied and unoccupied

orbitals included in the calculation, which were set to 6 and 8 respectively.

The mBSE approximation replaces the RPA dielectric function $\epsilon^{-1}(\mathbf{k})$ with an analytical model³⁵ and approximates the QP energies by applying a scissor operator (rigid shift) to the DFT results, aligning the direct band gap with that obtained from G_0W_0 calculations. This method has been successfully applied to other TMO perovskites^{21,28}. Its applicability to the present case was validated by comparison with the k -averaging^{20,51} and QP interpolation⁵⁰ approaches (see Supplementary Material).

III. RESULTS AND DISCUSSION

A. GW Electronic Properties

The calculated direct and indirect band gaps for both the cubic and tetragonal phases of PbTiO₃ computed at G_0W_0 level are reported in Table II. The complete band structures are shown in Fig. 1. As expected from previous studies^{41,52}, DFT severely underestimates the band-gap values, while the G_0W_0 results, which fall within the ranges reported in earlier works^{18,22}, provide a much more accurate description of the experimental values^{53–55}. The indirect band gap is located along the X–Z direction in k -space, while the direct gap occurs at the X point.

	This work		Literature	
	Indirect	Direct	Indirect	Direct
PBE	1.94	2.91	1.81 ⁵² /1.88 ⁴¹	2.95 ⁵²
GW	3.20	3.49	3.90 ²² /2.95 ¹⁸	-
Exp.				3.60 ⁵³ /3.45 ⁵⁴ /3.10 ⁵⁵

Table II: Calculated band-gaps, in eV, for the ferroelectric phase of PbTiO₃, using both DFT with PBE pseudopotentials and the G_0W_0 approximation. Computational and experimental results from the literature are also reported.

The band-gaps were also calculated in the G_0W_0 approximation for the structures of intermediate distortion, and are tabulated in Table III: while their values increase monotonically with distortion, their positions in k -space do not vary (see SM for results on over-distorted structures).

The first row of Figure 1 shows the band structures for both the paraelectric and ferroelectric phases of PbTiO₃, obtained using the DFT+scissor approximation and projected onto the relevant orbitals (p orbitals of the oxygen ions and t_{2g} , e_g orbitals of the titanium ion). These results were validated by comparison with band structures obtained using G_0W_0 calculations combined with Wannier interpolation^{56,57} (see SM).

As previously reported in the literature^{16,58}, the valence bands are predominantly composed of O- p states, while the conduction bands near the band gap are primarily determined by Ti- d states. The latter can be further divided into two contributions: the t_{2g} orbitals (d_{xy} , d_{xz} , and d_{yz}), located at lower energies, and the e_g orbitals (d_{z^2} and $d_{x^2-y^2}$), which appear

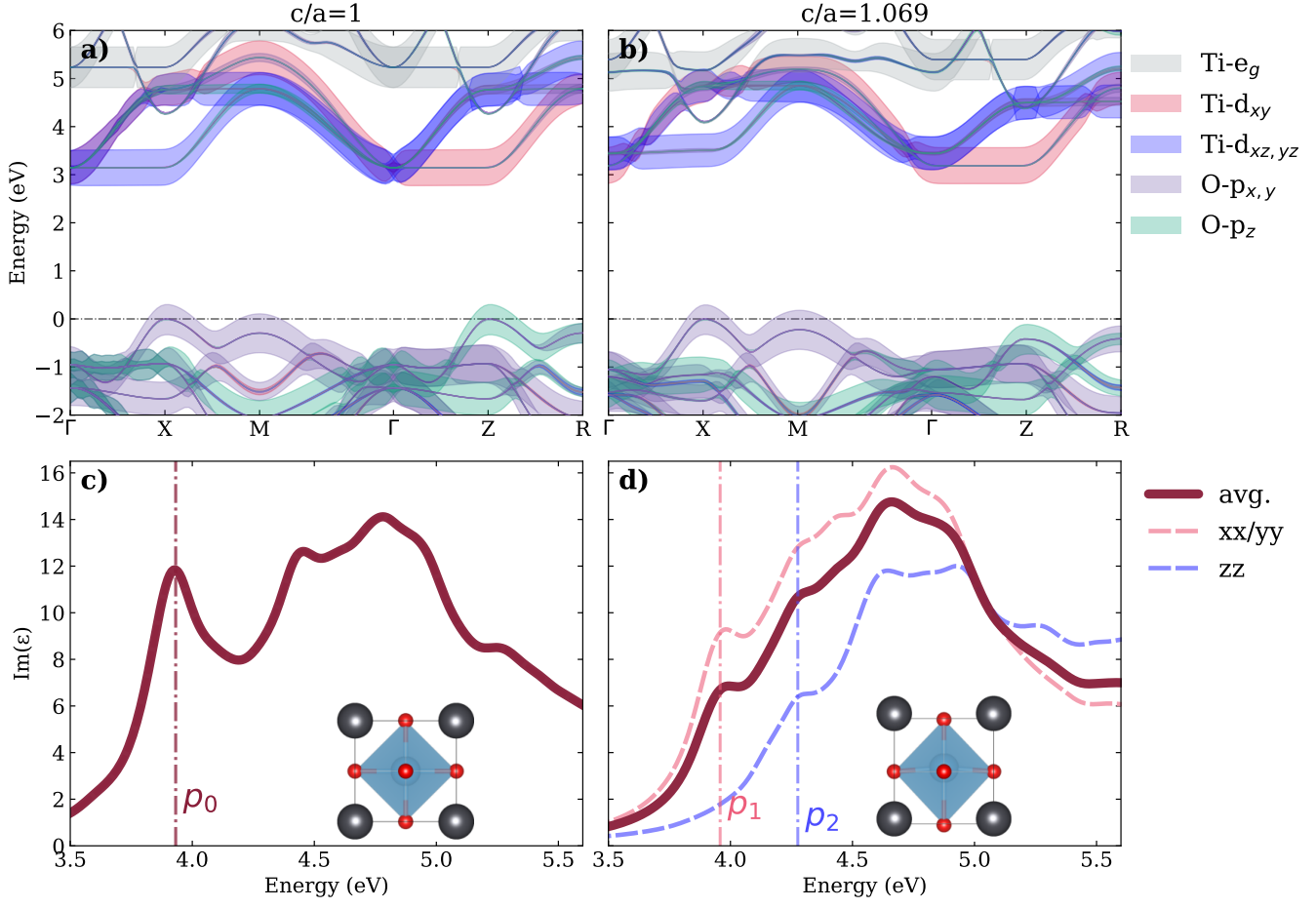


Figure 1: **a), b)** panels: band structures of the cubic and tetragonal phases of PTO projected on the orbitals of interest. The Fermi energy E_F is set to zero, while the arrows indicate the optical transitions and are coloured coded according to the spectral features they contribute to. **c), d)** panels: Corresponding mBSE optical absorption spectra. For the tetragonal phase, the xx/yy and zz components of the dielectric tensor are reported separately, along with the isotropic spectrum, calculated as an average among the components. The dashed vertical lines are located at the energies of the analysed peaks. Insets: Crystalline structure of the two phases of PTO. Pb ions in black, O in red, Ti in light blue.

Distortion	a [Å]	c/a	E_g^{ind} [eV]	E_g^{dir} [eV]	E_g^{opt} [eV]	E_{xb} [eV]	$E_{xb}^{(\text{nd})}$ [eV]	ϵ_∞^{-1}
0%	3.96	1	3.14	3.15	3.056	0.095	0.083	0.131
40%	3.95	1.027	3.14	3.19	3.097	0.098	0.086	0.132
60%	3.94	1.041	3.15	3.26	3.174	0.102	0.088	0.134
80%	3.93	1.055	3.18	3.36	3.280	0.107	0.090	0.136
100%	3.93	1.069	3.20	3.49	3.403	0.118	0.092	0.139

Table III: Lattice constant a , tetragonal distortion ratio c/a , indirect band gap E_g^{ind} , direct band gap E_g^{dir} , optical gap E_g^{opt} , exciton binding energy E_{xb} , first bright (non-dark) exciton binding energy $E_{xb}^{(\text{nd})}$, and inverse dielectric screening ϵ_∞^{-1} for the interpolated structures, as obtained from G_0W_0 and BSE calculations. The 100% and 0% data correspond to the ferroelectric (reference interpolated structure, see Tab. I) and paraelectric structures, respectively, as described in the text.

at higher energies. In both the paraelectric and ferroelectric phases, little mixing occurs between the t_{2g} and e_g states^{21,25,28}. For the paraelectric phase, the $\text{Ti-}t_{2g}$ manifold is threefold degenerate at Γ and contributes to the conduction-band minimum (CBM). In the ferroelectric tetragonal distortion, the Ti off-

centering enhances $\text{Ti-O } p\text{-}d$ hybridization, which plays a key role in stabilizing the ferroelectric phase, and alters the local crystal field, lifting the cubic t_{2g} degeneracy at Γ . As a result, the d_{xy} singlet lies at lower energies than the (d_{xz}, d_{yz}) doublet at Γ (Figure 1) and the magnitude of the energy splitting between

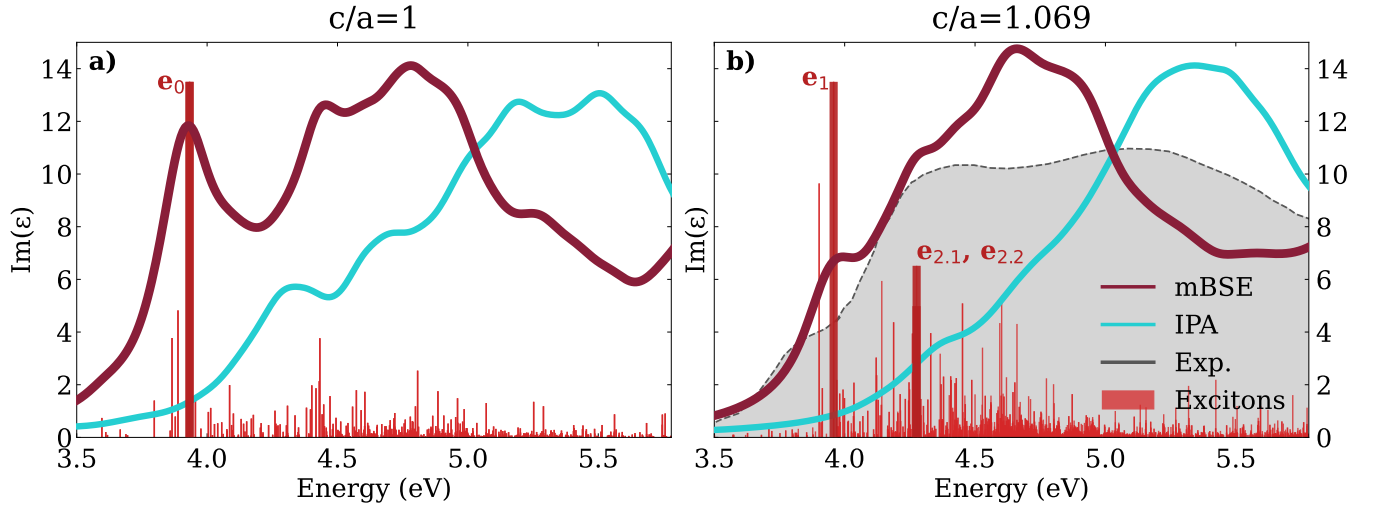


Figure 2: Isotropic optical absorption spectra for the paraelectric and ferroelectric structures obtained in the model-BSE and IPA (Independent Particle) approximations, together with the transition strengths of the main excitons. The excitons contributing to the peaks of interest are indicated by vertical (orange) lines and labelled (e).

tween the $\text{Ti-}d_{xz}/d_{yz}$ and d_{xy} states increases with increasing distortion amplitude.

Beyond the Γ point, the lowest conduction band along Γ -Z retains its predominant d_{xy} character and remains almost non-dispersive. In contrast, the corresponding band along Γ -X shifts to higher energies under the tetragonal distortion, consistent with the lifting of the t_{2g} degeneracy at Γ .

B. Absorption spectra

Table III summarizes the tetragonal distortion, band gaps, and key optical properties for all considered structures, including the optical gap E_g^{opt} , the binding energies E_{xb} of the first dark and non-dark (i.e., with nonzero transition strength) excitons as obtained from BSE calculations, and the static inverse dielectric screening ϵ_∞^{-1} . All these quantities are found to increase monotonically with increasing structural distortion. Moreover, the optical gap remains consistently lower than the G_0W_0 -calculated direct gap, confirming the presence of bound excitons. The second row of Figure 1 reports the absorption spectra (imaginary part of the dielectric function) for the cubic and tetragonal phases of PbTiO_3 , calculated within the mBSE approximation. The spectra are shown both as an average over all directions and with the components along the out-of-plane (zz) and in-plane (xx/yy) directions separated. In the cubic paraelectric phase, the isotropic spectrum presents a first prominent peak, labelled p_0 , at 3.93 eV. A feature at similar transition energies is also identifiable for the ferroelectric phase (labelled p_1), although with noticeably reduced oscillator strength. Crucially, this peak is visible only in the xx/yy component and is entirely absent in the out-of-plane response, which shows no trace of the corresponding excitation. Instead, the zz component develops a distinct shoulder around ~ 4.3 eV, labelled p_2 , which is not present in the cubic structure's spectra.

The importance of electron-hole interactions is highlighted in Figure 2. For the paraelectric structure in particular, excitonic effects induce a marked redshift and a substantial enhancement of the p_0 peak, consistent with trends reported for other cubic transition-metal-oxide perovskites^{19,28}. We also note that the introduction of the electron-hole interaction is necessary to obtain a good agreement for the onset of the experimental data,⁵⁹ see Figure 2 b).

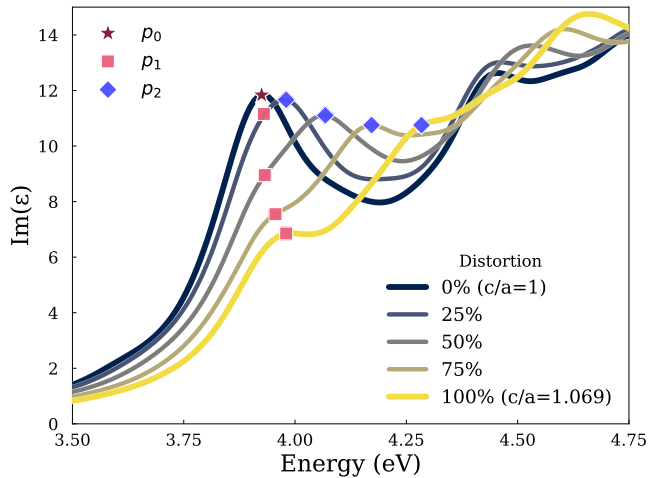


Figure 3: Isotropic optical absorption spectra for intermediate structures along the distortion from the paraelectric to the ferroelectric phase, obtained within the mBSE approximation. The marked peak positions highlight how the cubic p_0 feature progressively splits into the p_1 and p_2 branches as the polar distortion increases.

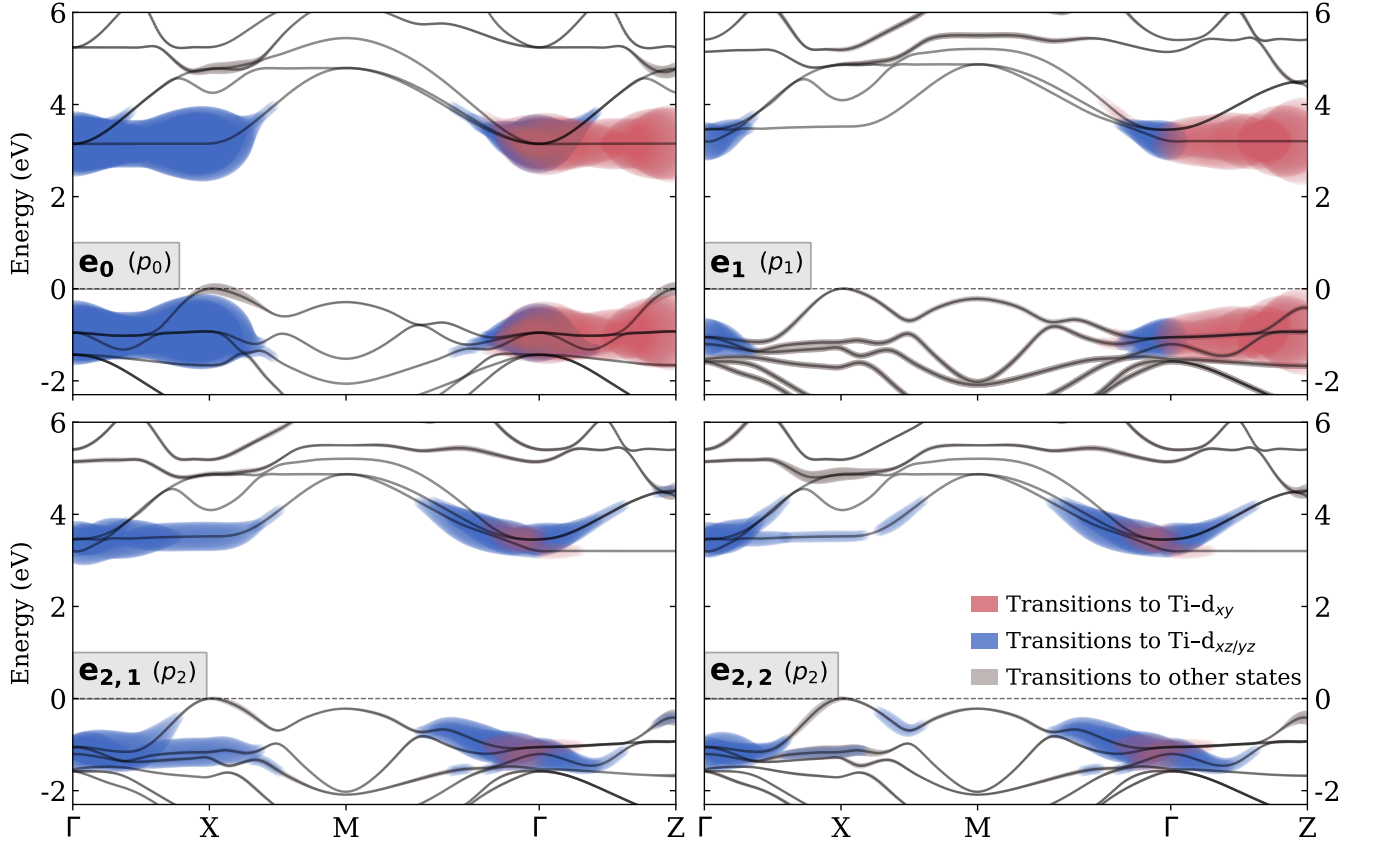


Figure 4: Fatband plots of the excitons from Figure 2: exciton e_0 from the paraelectric structure splits into three excitons with different characters in the ferroelectric phase. The black dots outline the band structure, while the coloured circles indicate the amplitude of the BSE eigenvector at each point. Different colours refer to different valence-conduction band pairs.

Having identified the key spectral peaks for both phases, we now move to the analysis of how the corresponding excitons couple to the progressive ferroelectric distortion and evolve across the structural transition.

For the paraelectric phase, the dominant contribution to the p_0 peak arises from a triple-degenerate excitonic state with a BSE eigenvalue of 3.393 eV (labelled e_0 in Figure 2). As shown by the fat-band analysis in Figure 4, the associated BSE eigenvectors display comparable weight along the Γ -Z and Γ -X directions, involving transitions From O-2p to Ti- dt_{2g} states, reflecting the cubic symmetry of the phase. Along these high-symmetry lines, the Ti- t_{2g} manifold remains nearly non-dispersive, reflecting the localized character of these states; a similar behaviour has been reported for other cubic perovskites and has been related to the strong enhancement of the absorption peak due to excitonic effects.^{19,28}

Figure 3 highlights the changes in the isotropic absorption spectrum when the tetragonal distortion is gradually turned on. The previously identified p_1 and p_2 peaks can be directly traced back to the distortion-driven splitting of the p_0 peak, which first broadens and then separates into two distinct branches as the distortion grows (becoming fully resolved for distortions beyond the experimental value; see SM). The splitting therefore introduces a distinct anisotropy in the dielectric response,

with p_1 confined to the in-plane (xx/yy) channel and entirely absent from the out-of-plane (zz) spectrum.

To clarify the microscopic origin of this anisotropy, we now examine the excitonic states associated with the split branches. The contribution to the lower energy branch p_1 is dominated by the doubly degenerate exciton e_1 shown in Figure 4 for the ferroelectric structure ($c/a = 1.069$) associated with a BSE eigenvalue of (3.96 eV). Other excitons lying close in energy also provide non-negligible oscillator strength, but their fat-band distributions are largely similar to that of e_1 . All of these states are doubly degenerate, consistent with them leading to a peak in the xx/yy degenerate component of the spectrum. The e_1 excitonic wavefunction possesses spectral weights almost entirely confined along the Γ -Z direction, primarily involving O- $p_{x,y} \rightarrow$ Ti- d_{xy} transition. Because these transitions carry dipole matrix elements predominantly in the in-plane direction, e_1 contributes primarily to the xx/yy component of the dielectric tensor, in line with the anisotropy observed for the p_1 peak.

The p_2 feature in the ferroelectric structure is related to two excitonic states, $e_{2,1}$ and $e_{2,2}$ with eigenvalues at 4.276 eV. Both excitons receive their predominant contributions from out-of-plane transitions from O- $2p_z$ to conduction Ti- d_{xz}/d_{yz} states. $e_{2,1}$ is doubly degenerate and has spectral weights mainly lo-

calised along $\Gamma - X$, albeit with much lower oscillator strengths compared to e_1 ; $e_{2,2}$ is instead predominantly localised at Γ and non-degenerate. These transitions carry dipole components with significant out-of-plane orientation, accounting for the appearance of spectral weight in the zz response around the energy of the p_2 feature. Lastly, the increasing p_1 – p_2 separation reflects the distortion-driven splitting of the Ti t_{2g} manifold. As the distortion grows, the energy separation between the Ti- d_{xy} and $d_{xz,yz}$ states increases. As discussed above, the lower-energy branch p_1 is dominated by in-plane transitions to the Ti- d_{xy} states (excitonic state e_1), whereas the higher-energy feature p_2 is associated with excitonic states with predominant transitions to Ti- $d_{xz,yz}$ states ($e_{2,1}$ and $e_{2,2}$). Consequently, the p_1 – p_2 separation increases with distortion, and the magnitude of the polar distortion therefore directly controls the energy splitting between the two features.

Overall, the picture is consistent with the peak observed in the cubic structure absorption spectrum (p_0) developing from a triple degenerate exciton that, under structural symmetry breaking, splits into doubly degenerate and non-degenerate excitation that give rise to two separate spectral features. As a consequence of this, the first absorption peak in the ferroelectric structures is not simply shifted compared to the one present in the paraelectric phase, but actually arises due to excitations of different nature.

IV. CONCLUSIONS

We have carried out a comprehensive *ab-initio* study of the electronic and optical properties of PbTiO₃ by combining G_0W_0 quasiparticle corrections with the solution of the Bethe-Salpeter equation, in the mBSE approximation, on a converged k -mesh. By interpolating between the cubic and tetragonal structures, we traced the continuous evolution of the electronic properties and optical spectrum as the ferroelectric distortion is progressively switched on. The indirect and direct band-gaps obtained for the ferroelectric phase of PTO are respectively 3.20 eV and 3.49 eV, falling within the previously reported ranges from GW and experimental studies.

Solving the BSE reveals, for the paraelectric structure, an absorption peak at 3.93 eV that is strongly enhanced by excitonic effects and evolves into two distinct spectral features as the polar distortion increases. By analysing the BSE eigenvectors in k -space, we show that the cubic structure peak is related to a triple degenerate exciton derived from transitions to d - t_{2g} states localised along $\Gamma - Z$ and $\Gamma - X$. Symmetry breaking partially lifts the degeneracy, giving rise to a doubly-degenerate lower excitonic state that contributes exclusively to the in-plane (xx/yy) dielectric channel, and a higher-energy set of excitonic states associated with the second spectral feature. This behavior follows directly from the different transition channels in the excitonic wavefunctions: in-plane $O-2p_{x,y} \rightarrow \text{Ti}-d_{xy}$ transitions for the lower branch and out-of-plane $O-2p_z \rightarrow \text{Ti}-d_{xz}/d_{yz}$ transitions for the higher branch. The polar distortion therefore introduces the in-plane/out-of-plane anisotropy and controls the energy separation between the two branches.

Beyond improving the accuracy of the first principles cal-

culations for the properties of paraelectric and ferroelectric lead titanate already reported in the literature, our work demonstrates that polar lattice distortions, tunable through external electric fields, provide a knob for tailoring the optical absorption spectrum of a ferroelectric perovskite, opening the door to novel applications in opto-electronical devices.

ACKNOWLEDGMENTS

The computational results have been achieved using the Austrian Scientific Computing (ASC) infrastructure.

AUTHOR DECLARATIONS

Conflict of Interest

The authors have no conflicts to disclose.

Author Contributions

Pietro Pacchioni: Investigation (lead); Data curation (lead); Formal analysis (equal); Writing – review & editing (equal). **Cesare Franchini:** Conceptualization (lead); Resources (lead); Supervision (equal); Formal analysis (equal); Methodology (supporting); Writing – review & editing (equal). **Lorenzo Varrassi:** Methodology (lead); Supervision (equal); Formal analysis (equal); Writing – review & editing (equal).

DATA AVAILABILITY

The data that support the findings of this study are available within the article and its supplementary material.

REFERENCES

- ¹R. von Helmolt, J. Wecker, B. Holzapfel, L. Schultz, and K. Samwer, “Giant negative magnetoresistance in perovskitelike $\text{La}_{2/3}\text{Ba}_{1/3}\text{MnO}_x$ ferromagnetic films,” *Physical Review Letters* **71**, 2331–2333 (1993).
- ²M. B. Salamon and M. Jaime, “The physics of manganites: Structure and transport,” *Reviews of Modern Physics* **73**, 583–628 (2001).
- ³K. Wang, J.-M. Liu, and Z. Ren, “Multiferroicity: the coupling between magnetic and polarization orders,” *Advances in Physics* **58**, 321–448 (2009).
- ⁴J. G. Bednorz and K. A. Müller, “Possible high T_c superconductivity in the BaLaCuO system,” *Zeitschrift für Physik B Condensed Matter* **64**, 189–193 (1986).
- ⁵Y. Tokura, “Correlated-Electron Physics in Transition-Metal Oxides,” *Physics Today* **56**, 50–55 (2003).
- ⁶S. C. Abrahams, S. K. Kurtz, and P. B. Jamieson, “Atomic Displacement Relationship to Curie Temperature and Spontaneous Polarization in Displacive Ferroelectrics,” *Physical Review* **172**, 551–553 (1968).
- ⁷M. J. Haun, E. Furman, S. J. Jang, H. A. McKinstry, and L. E. Cross, “Thermodynamic theory of PbTiO_3 ,” *Journal of Applied Physics* **62**, 3331–3338 (1987).
- ⁸A. Tawfik, O. M. Hemeda, A. M. A. Henaish, and A. M. Dorgham, “High piezoelectric properties of modified nano lead titanate zirconate ceramics,” *Materials Chemistry and Physics* **211**, 1–8 (2018).

- ⁹S. Zhang, H. Li, and M. Li, “Size-dependent piezoelectric coefficient d_{33} of PbTiO₃ nanoparticles,” *Materials Letters* **62**, 2438–2440 (2008).
- ¹⁰M. D. Fontana, F. Abdi, and K. Wojcik, “Electro-optical properties of a single domain PbTiO₃ crystal,” *Journal of Applied Physics* **77**, 2102–2106 (1995).
- ¹¹M. Veithen, X. Gonze, and P. Ghosez, “First-Principles Study of the Electro-Optic Effect in Ferroelectric Oxides,” *Physical Review Letters* **93**, 187401 (2004).
- ¹²R. Nishino, T. C. Fujita, F. Kagawa, and M. Kawasaki, “Evolution of ferroelectricity in ultrathin PbTiO₃ films as revealed by electric double layer gating,” *Scientific Reports* **10**, 10864 (2020).
- ¹³W. Ma and A. Hao, “Electric field-induced polarization rotation and ultrahigh piezoelectricity in PbTiO₃,” *Journal of Applied Physics* **115**, 104105 (2014).
- ¹⁴D. K. Fork, F. Armani-Leplingard, and J. J. Kingston, “Application of Electroceramic Thin Films to Optical Waveguide Devices,” *MRS Bulletin* **21**, 53–58 (1996).
- ¹⁵M.-Z. Wang, H.-J. Feng, C.-X. Qian, J. He, J. Feng, Y.-H. Cao, K. Yang, Z.-Y. Deng, Z. Yang, X. Yao, J. Zhou, S. F. Liu, and X. C. Zeng, “PbTiO₃ as Electron-Selective Layer for High-Efficiency Perovskite Solar Cells: Enhanced Electron Extraction via Tunable Ferroelectric Polarization,” *Advanced Functional Materials* **29**, 1806427 (2019).
- ¹⁶M. Yaseen, H. Ambreen, R. Mehmood, M. Iqbal, J. Iqbal, T. Alshahrani, S. Noreen, and A. Laref, “Investigation of optical and thermoelectric properties of PbTiO₃ under pressure,” *Physica B: Condensed Matter* **615**, 412857 (2021).
- ¹⁷S. M. Hosseini, T. Movlaroooy, and A. Kompany, “First-principles study of the optical properties of PbTiO₃,” *The European Physical Journal B* **46**, 463–469 (2005).
- ¹⁸L. Bendaoudi, T. Ouahrani, A. Daouli, B. Rerbal, R. M. Boufatah, A. Morales-García, R. Franco, Z. Bedrane, M. Badawi, and D. Errandonea, “Electronic and electrocatalytic properties of PbTiO₃: unveiling the effect of strain and oxygen vacancy,” *Dalton Transactions* **52**, 11965–11980 (2023).
- ¹⁹L. Sponza, V. Vénard, F. Sottile, C. Giorgetti, and L. Reining, “Role of localized electrons in electron-hole interaction: The case of SrTiO₃,” *Physical Review B* **87**, 235102 (2013).
- ²⁰P. Liu, B. Kim, X.-Q. Chen, D. D. Sarma, G. Kresse, and C. Franchini, “Relativistic GW+BSE study of the optical properties of ruddlesden-popper iridates,” *Physical Review Materials* **2**, 075003 (2018).
- ²¹V. Begum, M. E. Gruner, and R. Pentcheva, “Role of the exchange-correlation functional on the structural, electronic, and optical properties of cubic and tetragonal srTiO₃ including many-body effects,” *Physical Review Materials* **3**, 065004 (2019).
- ²²G. Y. Gou, J. W. Bennett, H. Takenaka, and A. M. Rappe, “Post density functional theoretical studies of highly polar semiconductive Pb(Ti_{1-x}Ni_x)O_{3-x} solid solutions: Effects of cation arrangement on band gap,” *Physical Review B* **83**, 205115 (2011).
- ²³J. Klimeš, M. Kaltak, and G. Kresse, “Predictive GW calculations using plane waves and pseudopotentials,” *Physical Review B* **90**, 075125 (2014).
- ²⁴J. He and C. Franchini, “Structural determination and electronic properties of the 4d perovskite srPdo₃,” *Phys. Rev. B* **89**, 045104 (2014).
- ²⁵Z. Ergönenc, B. Kim, P. Liu, G. Kresse, and C. Franchini, “Converged G W quasiparticle energies for transition metal oxide perovskites,” *Physical Review Materials* **3**, 024601 (2018).
- ²⁶K.-G. Lim and K.-H. Chew, “Dynamics of ferroelectric polarization and internal electric field in PbTiO₃/SrTiO₃ superlattices,” *Ferroelectrics* **586**, 109–120 (2021).
- ²⁷J. Zhai, X. Yao, and L. Zhang, “The ferroelectric and antiferroelectric behavior of PbTiO₃/PbZrO₃-multilayered thin films,” *Ceramics International* **30**, 1263–1266 (2004).
- ²⁸L. Varrassi, P. Liu, Z. E. Yavas, M. Bokdam, G. Kresse, and C. Franchini, “Optical and excitonic properties of transition metal oxide perovskites by the Bethe-Salpeter equation,” *Physical Review Materials* **5**, 074601 (2021).
- ²⁹F. Jia, G. Kresse, C. Franchini, P. Liu, J. Wang, A. Stroppa, and W. Ren, “Cubic and tetragonal perovskites from the random phase approximation,” *Phys. Rev. Mater.* **3**, 103801 (2019).
- ³⁰L. Varrassi, F. Ellinger, E. Flage-Larsen, M. Wolloch, G. Kresse, N. Marzari, and C. Franchini, “Automated workflow for accurate high-throughput gw calculations using plane waves,” *npj Computational Materials* **11**, 351 (2025).
- ³¹S. Albrecht, L. Reining, R. Del Sole, and G. Onida, “Ab Initio Calculation of Excitonic Effects in the Optical Spectra of Semiconductors,” *Physical Review Letters* **80**, 4510–4513 (1998).
- ³²G. Onida, L. Reining, and A. Rubio, “Electronic excitations: density-functional versus many-body Green’s-function approaches,” *Reviews of Modern Physics* **74**, 601–659 (2002).
- ³³F. Bechstedt, R. Del Sole, G. Cappellini, and L. Reining, “An efficient method for calculating quasiparticle energies in semiconductors,” *Solid State Communications* **84**, 765–770 (1992).
- ³⁴F. Fuchs, J. Furthmüller, F. Bechstedt, M. Shishkin, and G. Kresse, “Quasiparticle band structure based on a generalized Kohn-Sham scheme,” *Physical Review B* **76**, 115109 (2007).
- ³⁵M. Bokdam, T. Sander, A. Stroppa, S. Picozzi, D. D. Sarma, C. Franchini, and G. Kresse, “Role of Polar Phonons in the Photo Excited State of Metal Halide Perovskites,” *Scientific Reports* **6**, 28618 (2016).
- ³⁶L. Varrassi, P. Liu, and C. Franchini, “Quasiparticle and excitonic properties of monolayer srTiO₃,” *Phys. Rev. Mater.* **8**, 024001 (2024).
- ³⁷G. Kresse and J. Hafner, “Ab initio molecular dynamics for liquid metals,” *Physical Review B* **47**, 558–561 (1993).
- ³⁸G. Kresse and J. Furthmüller, “Efficient iterative schemes for ab initio total-energy calculations using a plane-wave basis set,” *Physical Review B* **54**, 11169–11186 (1996).
- ³⁹P. E. Blöchl, “Projector augmented-wave method,” *Physical Review B* **50**, 17953–17979 (1994).
- ⁴⁰J. P. Perdew, K. Burke, and M. Ernzerhof, “Generalized Gradient Approximation Made Simple,” *Physical Review Letters* **78**, 1396–1396 (1997).
- ⁴¹Y. Zhang, J. Sun, J. P. Perdew, and X. Wu, “Comparative first-principles studies of prototypical ferroelectric materials by LDA, GGA, and SCAN meta-GGA,” *Physical Review B* **96**, 035143 (2017).
- ⁴²A. Yoshiasa, T. Nakatani, A. Nakatsuka, M. Okube, K. Sugiyama, and T. Mashimo, “High-temperature single-crystal X-ray diffraction study of tetragonal and cubic perovskite-type PbTiO₃ phases,” *Acta Crystallographica Section B Structural Science, Crystal Engineering and Materials* **72**, 381–388 (2016).
- ⁴³R. Nelmel and W. Kuhs, “The crystal structure of tetragonal PbTiO₃ at room temperature and at 700 K,” *Solid State Communications* **54**, 721–723 (1985).
- ⁴⁴G. Shirane, R. Pepinsky, and B. C. Frazer, “X-ray and neutron diffraction study of ferroelectric PbTiO₂,” *Acta Crystallographica* **9**, 131–140 (1956).
- ⁴⁵S. A. Mabud and A. M. Glazer, “Lattice parameters and birefringence in PbTiO₃ single crystals,” *Journal of Applied Crystallography* **12**, 49–53 (1979).
- ⁴⁶M. Shishkin and G. Kresse, “Implementation and performance of the frequency-dependent GW method within the PAW framework,” *Physical Review B* **74**, 035101 (2006).
- ⁴⁷R. Del Sole, L. Reining, and R. W. Godby, “GWT approximation for electron self-energies in semiconductors and insulators,” *Physical Review B* **49**, 8024–8028 (1994).
- ⁴⁸S. Albrecht, L. Reining, G. Onida, V. Olevano, and R. Del Sole, “Albrecht et al. Reply,” *Physical Review Letters* **83**, 3971–3971 (1999).
- ⁴⁹F. Fuchs, C. Rödl, A. Schleife, and F. Bechstedt, “Efficient $\mathcal{O}(N^2)$ approach to solve the Bethe-Salpeter equation for excitonic bound states,” *Physical Review B* **78**, 085103 (2008).
- ⁵⁰D. Kammerlander, S. Botti, M. A. L. Marques, A. Marini, and C. Attaccalite, “Speeding up the solution of the Bethe-Salpeter equation by a double-grid method and Wannier interpolation,” *Physical Review B* **86**, 125203 (2012).
- ⁵¹T. Sander, E. Maggio, and G. Kresse, “Beyond the Tamm-Dancoff approximation for extended systems using exact diagonalization,” *Physical Review B* **92**, 045209 (2015).
- ⁵²A. Jain, G. Hautier, C. J. Moore, S. Ping Ong, C. C. Fischer, T. Mueller, K. A. Persson, and G. Ceder, “A high-throughput infrastructure for density functional theory calculations,” *Computational Materials Science* **50**, 2295–2310 (2011).
- ⁵³V. I. Zametin, “Absorption Edge Anomalies in Polar Semiconductors and Dielectrics at Phase Transitions,” *physica status solidi (b)* **124**, 625–640 (1984).
- ⁵⁴C. H. Peng, J.-F. Chang, and S. B. Desu, “Optical Properties of PZT, PLZT, and PNZT Thin Films,” *MRS Online Proceedings Library* **243**, 21–26 (1991).

- ⁵⁵H. Lemziouka, L. E. H. Omari, R. Moubah, A. Boutahar, S. Bahhar, M. Abid, and H. Lassri, "Structural, dielectric and optical properties of Cu-doped PbTiO₃ ceramics prepared by sol-gel," *Materials Today: Proceedings The International Conference on Water Depollution and Green Energy 2019*, **37**, 3940–3945 (2021).
- ⁵⁶A. A. Mostofi, J. R. Yates, G. Pizzi, Y.-S. Lee, I. Souza, D. Vanderbilt, and N. Marzari, "An updated version of wannier90: A tool for obtaining maximally-localised wannier functions," *Computer Physics Communications* **185**, 2309–2310 (2014).
- ⁵⁷C. Franchini, R. Kováčik, M. Marsman, S. Sathyanarayana Murthy, J. He, C. Ederer, and G. Kresse, "Maximally localized wannier functions in lamno3 within pbe + u, hybrid functionals and partially self-consistent gw: an efficient route to construct ab initio tight-binding parameters for eg perovskites," *Journal of Physics: Condensed Matter* **24**, 235602 (2012).
- ⁵⁸I. Derkaoui, M. Achehboune, R. I. Eglitis, A. I. Popov, and A. Rezzouk, "Overview of the Structural, Electronic and Optical Properties of the Cubic and Tetragonal Phases of PbTiO₃ by Applying Hubbard Potential Correction," *Materials* **16**, 4302 (2023).
- ⁵⁹T. D. Kang, H. Lee, G. Xing, N. Izumskaya, V. Avrutin, B. Xiao, and H. Morkoç, "Dielectric functions and critical points of pbtio3, pbzro3, and pbzr0.57ti0.43o3 grown on srto3 substrate," *Applied Physics Letters* **91**, 022918 (2007).

SUPPLEMENTARY MATERIALS

Further distorted structures

As mentioned in Section II of the main text, performing relaxation using PBE functionals leads to overestimating the tetragonal distortion of TMO perovskites, thus only the interpolated structures with tetragonal distortion up to the experimental value were analyzed in detail.

Table IV extends Table III of the main text with further ferroelectric structures up to a distortion of 320%, where 100% corresponds to the experimental structure. The trends discussed in Section III B continue even for these unphysical structures, except for the direct band-gap E_g^{dir} which abruptly decreases for the most elongated, which also leads to the breakdown of the scissor approximation in this extreme case.

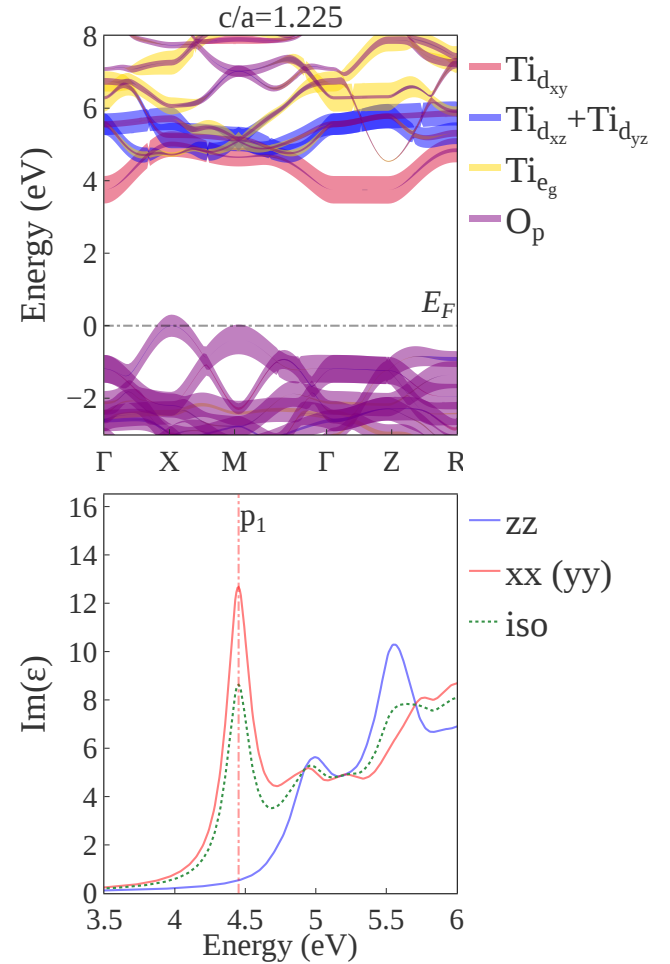


Figure 5: Equivalent of Figure 1 for the 320% distorted structure.

Nonetheless, significant differences can be found in the band structures and optical absorption spectra. For instance, Figure 5, reports the projected band structure and imaginary part of the dielectric function for the most distorted structure. It can be noticed that the bands present significant more distortion

then previously observed, and that significant mixing between the e_g and t_{2g} contributions arises. As expected from the rising optical band gap, the first absorption peak is further redshifted, but the second peak discussed in the main text is not discernible any-more, possibly due to the macroscopically changed and more complicated electronic structure, or simply because it now resides outside the converged zone.

Scissor approximation accuracy

Owing to the extreme computational cost of performing G_0W_0 calculations on a k -grid dense enough to obtain converged optical absorption spectra, the scissor approximation was employed instead. This consist in calculating the direct band gaps at both the PBE and G_0W_0 level with a less dense grid ($6 \times 6 \times 6$ in our case), finding the difference and then apply a corresponding rigid shift upwards to the valence bands obtained on a denser grid with PBE. This approach is evidently only valid if the quasiparticle corrections do not significantly alter the shape itself of the bands, but only their energy.

To verify this assumption, the full band structures of the extremal structures (0% and 320% distortion) were found starting from the G_0W_0 data using the Wannier interpolation method, as implemented by Wannier90⁵⁶. Their comparison to properly shifted, PBE bands is presented in Figure 6. The optically active bands of the cubic structure that are considered in the main text correspond almost perfectly, while a significant difference is present in the case of the overly distorted structure near the X k -point, explaining the abrupt decrease in the direct band gap.

The scissor approximation is thus expected to produce the

correct optical properties for the cubic and first distorted structures, but may result in inaccuracies when applied to the unphysical cases discussed in the previous section.

model-BSE accuracy

As discussed in the main text, the model-BSE approximation replaces the RPA dielectric function with an analytical model, and it has been validated on other TMO perovskites. However, its applicability is not universal, and it is therefore important to verify its accuracy in the case of PTO.

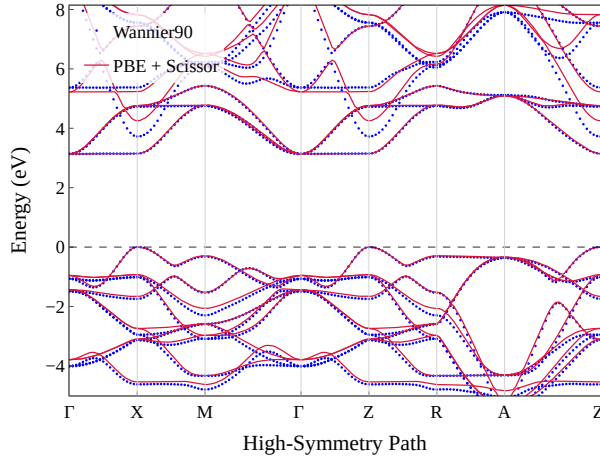
Since we were not able to perform full BSE calculations using the parameters required for convergence, we resorted to two other approximation methods already present in the literature: k -averaging and QP interpolation.

Given an $N \times N \times N$ target grid, the first approach requires first generating an $n \times n \times n$ base grid, made up of points at positions in reciprocal space K_n with weights W_n , then performing BSE calculations on $m \times m \times m$ grids each centred at one K_n , where m is such that $N = m \times n$. A weighted average is then performed over the dielectric functions. We applied this method only to the 320% distorted structure, and we took $n = 4$, $m = 6$.

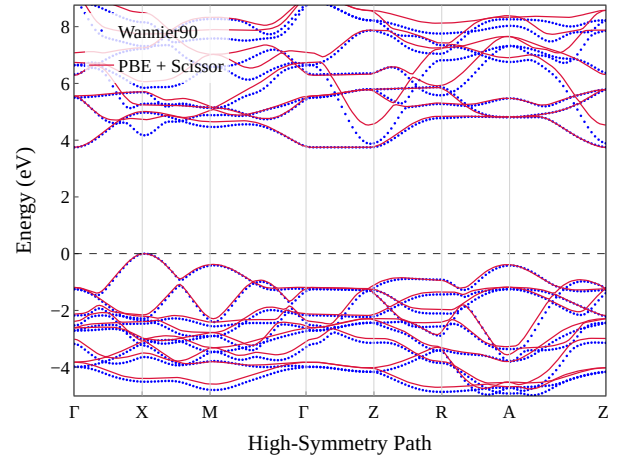
The absorption spectra resulting from the three approximations are compared in Figure 7. Despite quantitative differences being present, especially for the cubic structure, the overall picture is consistent, as the position and shape of the peaks is constant, suggesting that the nature of the underlying excitations does not change. mBSE thus remains a valid, computationally approachable method to study the optical properties of PTO as its tetragonal distortion is varied.

Distortion	a [Å]	c/a	E_g^{ind} [eV]	E_g^{dir} [eV]	E_g^{opt} [eV]	E_{xb} [eV]	$E_{xb}^{(nd)}$ [eV]	ϵ_∞^{-1}
0%	3.96	1	3.14	3.15	3.056	0.095	0.083	0.131
40%	3.95	1.027	3.14	3.19	3.097	0.098	0.086	0.132
60%	3.94	1.041	3.15	3.26	3.174	0.102	0.088	0.134
80%	3.93	1.055	3.18	3.36	3.280	0.107	0.090	0.136
100%	3.93	1.069	3.20	3.49	3.403	0.118	0.092	0.139
120%	3.92	1.083	3.23	3.63	3.543	0.132	0.094	0.141
160%	3.90	1.111	3.30	3.97	3.836	0.144	0.102	0.147
240%	3.87	1.167	3.49	4.25	4.223	0.172	0.153	0.161
320%	3.84	1.225	3.75	4.17	4.448	0.271	0.271	0.177

Table IV: Lattice constant a , tetragonal distortion ratio c/a , indirect band gap E_g^{ind} , direct band gap E_g^{dir} , optical gap E_g^{opt} , exciton binding energy E_{xb} , first bright (non-dark) exciton binding energy $E_{xb}^{(nd)}$, and inverse dielectric screening ϵ_∞^{-1} for the interpolated structures, as obtained from G_0W_0 and BSE calculations, including the overly distorted structures. The 320% data corresponds to the relaxed structured obtained with PBE functionals.



(a) Cubic structure



(b) Overly distorted tetragonal structure

Figure 6: Comparison between the band structures of the 0% and 320% distorted PTO structures calculated using Wannier interpolation on G_0W_0 data or by applying the scissor approximation to the PBE results.

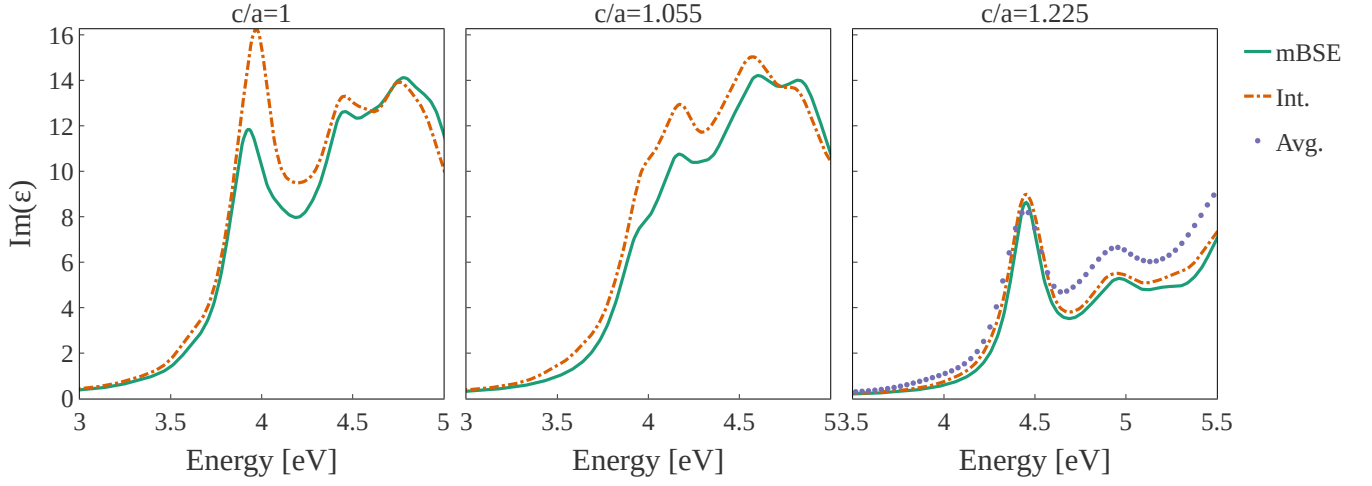


Figure 7: Averaged optical absorption spectra for three structures of different distortion obtained in the model-BSE approximation and through the QP interpolation method. The results of the averaging method on a $24 \times 24 \times 24$ k -grid are also shown for the most distorted structure.